Interface modulation of MoS_2/metal oxide heterostructures for efficient hydrogen evolution electrocatalysis

Jue Hu, Chengxu Zhang, Yizhen Zhang, Baomin Yang, Qianglong Qi, Mingzi Sun, Futing Zi, Michael K. H. Leung*, and Bolong Huang**

Prof. J. H., Prof. C. Z., B. Y., Q. Q. and F. Z.

Faculty of Science, Kunming University of Science and Technology, Kunming, 650093 China
E-mail: hujue@kust.edu.cn

Y. Z. and Prof. M. K. H. L.

Ability R&D Energy Research Centre, School of Energy and Environment, City University of Hong Kong, Hong Kong SAR, 999077 China

E-mail: mkh.leung@cityu.edu.hk

Prof. M. K. H. L.

The City University of Hong Kong Shenzhen Research Institute, Shenzhen, Guangdong, 5180 00 China

M. S. and Prof. B. H.

Department of Applied Biology and Chemical Technology, The Hong Kong Polytechnic University, Hung Hom, Kowloon, Hong Kong SAR, 999077 China

Email: bhuang@polyu.edu.hk

Keywords: Hydrogen evolution reaction; MoS_2/metal oxides heterostructures; interface modulation; reaction kinetics; alkaline environment

Developing efficient earth-abundant MoS_2 based hydrogen evolution electrocatalysts is important but still challenging due to the disappointingly sluggish kinetics in alkaline media. Herein, for the first time, a strategy to fabricating high-performance MoS_2 based hydrogen evolution electrocatalyst by modulating interface electronic structure via metal oxides is

developed. All the heterostructure catalysts present significant improvement of the HER electrocatalytic activities compared to their bare components, demonstrating a positive role of metal oxides decoration in promoting the rate-limited water dissociation step for HER mechanism in alkaline media. The as-obtained MoS_2/Ni_2O_3H catalyst exhibits a low overpotential of 84 mV at 10 mA/cm^2 and small charge-transfer resistance of 1.5 Ω in 1 M KOH solution. The current density (217 mA/cm^2) at the overpotential of 200 mV is about 2 and 24 times higher than that of commercial Pt/C and bare MoS_2 catalysts, respectively. Additionally, these MoS_2/metal oxides heterostructure catalysts show outstanding long-term stability under harsh chronopotentiometry test. Density function theory calculation reveals the varied sensitivity of 3d-band in different transition oxides, in which Ni-3d of Ni_2O_3H has been evidentially activated to achieve the fast electron transfer for HER as the electron-depletion center. Both electronic properties and energetic reaction trends confirmed the high electroactivity of MoS_2/Ni_2O_3H in the adsorption and dissociation of H_2O for highly efficient HER in the alkaline media.

In a world with rising concern about energy security, environmental crisis and global warming, creating a fossil-fuel-free and renewable energy system while preserving our environment is one of the most crucial challenges facing humanity today.[1-6] Hydrogen (H_2), with the highest mass specific energy density (140 MJ/kg) among the currently known or used fuels and carbon-emission-free characteristic since water is the sole product from its oxidation reaction, has been considered as a promising fuel to replace the dwindling fossil fuels and the most likely fuel of the future.[7-8] Hydrogen evolution from water by electrolysis which would allow for the storage of renewable energy in hydrogen has been suggested as one of the most efficient, sustainable and fossil-free ways to produce highly pure hydrogen on a large scale.[9]

Generally, the electrolysis of water consists of two half reactions: the cathodic hydrogen evolution reaction (HER) and anodic oxygen evolution reaction (OER). It is well known that the water splitting in alkaline electrolytes are crucial in terms of the popular water-alkali and chlor-alkali electrolyzes and the potential to forego noble metal electrocatalysts for both OER and HER.[10-11] However, the HER kinetics is disappointingly sluggish in alkaline electrolytes, i.e., at least two orders of magnitude slower than in acidic ones, for example on the benchmarked Pt catalyst surfaces.[12-13]

To obtain the catalysts with high HER activity in the alkaline environment, it is essential to understand the reason for this puzzling difference of HER kinetics in acid and base.[14-15] Hydrogen evolution reaction is commonly believed to consist a combination of two elementary pathways: Volmer-Tafel pathway or Volmer-Heyrovsky pathway, including the electrochemical adsorption of H^+ in acid or cleavage of HO–H bond in H_2O in base (Volmer step), electrochemical desorption of H_2 in acid or cleavage of HO–H bond and then electrochemical desorption of H_2 in base (Heyrovsky step), and chemical desorption of H_2 (Tafel step).[7, 16-18] Based on these different expressions of HER in acid and base, it is obvious that the dissociation of water is crucial for HER in the alkaline environment.[19] Markovic and co-workers first reported an inspiring bifunctional HER mechanism in an alkaline solution. They demonstrated a decisive role of adsorbed hydroxyl species (OH_{ad}) in the HER reaction metal hydroxyl ($Ni(OH)_2$) decorated Pt surfaces, and suggested that the HER is controlled by both the substrate-H_{ad} and substrate-OH_{ad} energetics.[7, 20-21] More recently, Huang and co-workers demonstrated a synergistic effect of the Pt_3Ni/NiS interface where NiS promoting water dissociation and Pt_3Ni enhancing H_{ad} combination.[22] Despite their high efficiency, the widespread use of noble metals as catalysts is significantly limited by their high cost and

scarcity in nature.[23] Thus, it is highly desirable to find suitable alternatives to noble metal catalysts that are composed of inexpensive and earth-abundant elements for HER electrocatalysis.

Herein, we take the advantage of the earth-abundant MoS_2 which is good at adsorption and recombination of hydrogen intermediates (H_{ad}) and metal oxides, i.e. Ni_2O_3H, Co_3O_4 and Fe_2O_3, which are effective for cleaving the HO–H bond,[20, 24-25] to create a class of MoS_2/metal oxide heterostructures for facilitating different parts of the overall multistep of HER process in alkaline electrolytes. The flexible modulation of HER performance of composite interfaces is achieved by the precise selection of the transition oxides, in which the 3d-band of Ni in MoS_2/Ni_2O_3H has been substantially activated as the "electron pump" to achieve remarkable HER performance in the base environment. The optimized MoS_2/Ni_2O_3H composite yields the highest HER activity with an overpotential as low as 84 mV at 10 mA/cm^2 in alkaline electrolyte, which is 120 mV lower than that of the pure MoS_2 catalyst. The current density at the overpotential of 200 mV is 217 mA/cm^2, which is 2 times higher than that of the commercial Pt/C catalyst in alkaline media, indicating a superior catalyst to most previously reported earth abounded HER catalysts.

Results and discussion

The kinetically favorable HER catalysts in alkaline media should possess a well-designed interface for facilitated H_2O adsorption, water dissociation and recombination of hydrogen intermediates (H_{ad}). In this light, we applied the density function theory (DFT) to analyze the electronic structure of the MoS_2/Ni_2O_3H, MoS_2/Co_3O_4, and MoS_2/Fe_2O_3 composites. The electroactive bonding and anti-bonding orbitals of the interface near the Fermi level (E_F) are

illustrated to emphasize the electronic modulations. Apparently, the electronic distribution on MoS_2/Ni_2O_3H is mainly located on the interface. In comparison, the interface in MoS_2/Co_3O_4 and MoS_2/Fe_2O_3 show slightly less concentrated electronic distribution. The evident strain is observed at the interface region, which leads to the structure distortion. The optimal adsorbed sites for the key intermediate H_2O are the transition metal sites near the interface, respectively. This predicts the high electroactivity of the interface region (**Figure 1A-C**).

The interface modulations of the oxides are reflected by the projected partial density of states (PDOS). The interfacial Ni site acts as a highly active "electron pump" close to the Fermi level (E_F). The t_{2g}-e_g gap is significantly minimized and the e_g state obviously across E_F in the MoS_2/Ni_2O_3H interface indicates the high electroactivity for electron-transfer. In comparison, the t_{2g}-e_g splitting effects have been substantially enhanced within the interface region in both MoS_2/Co_3O_4 and MoS_2/Fe_2O_3, indicating a larger barrier for the t_{2g}-e_g electron-transfer. The Mo-4d band in pristine MoS_2 has shown a similar gap size for electron transfer with MoS_2/Fe_2O_3 **(Figure 1D**). We further interpret the electronic contributions given by different regions in the interface models. For MoS_2/Ni_2O_3H, the evolution of PDOS from Ni in the MoS_2/Ni_2O_3H substantially shifted towards the E_F as closer to the interface region. The dominant peak of Ni-3d has shifted from E_V- 3.0 eV to E_V- 1.0 eV (**Figure 1E**). Co-3d bands in Co_3O_4 occupy a close position to E_F, supporting the electroactivity in pristine Co_3O_4 in experiments. The shifting of the 3d-bands is not evident in the interface region (**Figure 1F**). The t_{2g}-e_g splitting is essential to determine the electron transfer between the catalyst surface and the p-p lone pair electrons in molecules such as H_2O, OH in the alkaline HER. Thus, although the 3d-bands evolution of Fe in MoS_2/Fe_2O_3 is similar to the Ni in MoS_2/Ni_2O_3H,

the strong t_{2g}-e_g splitting even near the interface region would largely constraint the HER performance (**Figure 1G**).

Aligned molybdenum sulfide (MoS_2) nanosheet arrays were prepared by the microwave hydrothermal method. This process leads to the uniform formation of ultrathin MoS_2 nanosheets with an average wide of ~10 nm and length of ~700 nm on carbon fiber paper (CFP) surface (**Figure S1**). Each individual nanosheet is perpendicular to the CFP substrate indicating abundantly exposed edges, which is similar to our previously reported works.[24]. The hierarchical MoS_2/Ni_2O_3H, MoS_2/Co_3O_4 and MoS_2/Fe_2O_3 composites were synthesized by directly growing the Ni_2O_3H, Co_3O_4 and Fe_2O_3, respectively, on the surface of the MoS_2 nanosheet arrays via the second hydrothermal reaction at 120 ºC for 12 h. Surface morphologies of the MoS_2/Ni_2O_3H sample are depicted by the field-emission scanning electron microscopy (FESEM) images shown in Figure 2. From the micrometer-scale view of SEM images in **Figure 2A** and **Figure S2**, it is evident that the surface of the MoS_2 is fully and uniformly covered with Ni_2O_3H nanosheets, which is different from the nanosheets morphology of MoS_2. SEM-energy dispersive X-ray spectroscopy (SEM-EDS) mapping of the MoS_2/Ni_2O_3H composite reveals that Ni, Mo, S and O are uniformly distributed within the large SEM scope of view (**Figure S3**). Transmission electron microscopy (TEM) images further manifest the nanosheet feature on the MoS_2/Ni_2O_3H composite (**Figure 2C**). As revealed by the high-resolution TEM (HRTEM) image and the corresponding fast Fourier transformation (FFT) patterns in **Figure 2D**, the well defined Ni_2O_3H phase with lattice space of 0.25 nm for (101) facet is closely connected with the MoS_2 lattice, showing clear boundaries between the Ni_2O_3H and MoS_2. TEM-EDS elemental mappings show that the

uniform distribution of Mo, S for MoS_2 nanosheets which combined with Ni in Ni_2O_3H sheet and exposed MoS_2/Ni_2O_3H interfaces (**Figure 2E**).

To analyze the morphology of the MoS_2/Co_3O_4 and MoS_2/Fe_2O_3 samples, FESEM and HRTEM images were shown in Figure 2 and Figure S4-9. The MoS_2/Co_3O_4 heterostructures consist of inner MoS_2 covered by Co_3O_4 nanosheets (**Figure S6**). Different from the morphology of Ni_2O_3H nanosheets, Co_3O_4 nanosheets with the thickness and size of 50-80 nm and 300-2000 nm (**Figure S4**), respectively, gather together to assemble nanosheet flowers. The FESEM images in **Figure S9** show that the MoS_2/Fe_2O_3 composite is composed of a particle-like structure of Fe_2O_3 on the edge surfaces of the MoS_2 sheet arrays[26]. The SEM-EDS mappings (in **Figure S5** and **S8**) show that the Co and Fe elements are mainly distributed over the Co_3O_4 nanosheets and Fe_2O_3 nanoparticles, respectively. The highly ordered lattice planes in the HRTEM image of MoS_2/Co_3O_4 composite are clearly visible in **Figure 2E**. Lattice fringes with the distances of 0.63 nm and 0.246 nm corresponded to the (002) facet of MoS_2 and (311) facet of Co_3O_4, respectively. In **Figure 2G**, the d-spacing of 0.63 nm and 0.37 nm, which corresponds to the (002) facet of MoS_2 and (012) facet of Fe_2O_3 crystals, respectively. These suggest the formation of interfaces between the (002) facet of MoS_2 and the (311) facet of Co_3O_4 for MoS_2/Co_3O_4 composite, and (002) facet of MoS_2 and the neighboring (012) facet of Fe_2O_3 in the MoS_2/Fe_2O_3 composite. Element mapping and corresponding energy dispersive X-ray (EDX) images shown in **Figure S6** and **S9** of the MoS_2/Co_3O_4 and MoS_2/Fe_2O_3 composites, respectively, present the uniform distribution of Mo, S for MoS_2 nanosheets which combined with Co in Co_3O_4 and Fe in Fe_2O_3.

Extensive physical characterization was conducted to further reveal the structure of the MoS_2/Ni_2O_3H, MoS_2/Co_3O_4 and MoS_2/Fe_2O_3 composites. **Figure 3A-C** show the X-ray diffraction (XRD) patterns of the MoS_2, MoS_2/Ni_2O_3H, MoS_2/Co_3O_4 and MoS_2/Fe_2O_3 composite samples. The diffraction peaks at 2θ = 13.98°, 33.46° and 58.96° in the MoS_2, MoS_2/Ni_2O_3H, MoS_2/Co_3O_4 and MoS_2/Fe_2O_3 samples correspond to the (002), (100) and (110) planes of 2H-MoS_2 crystal, respectively. In comparison with the XRD pattern of bare MoS_2, typical XRD peaks at 11.7°, 21.9°, 25.2°, 35.9°, 44.3°, 54.6° and 63.6° are also observed in **Figure 3A** and **Figure S10A**, which correspond to the (020), (120), (040), (101), (141), (214) and (301) planes of Ni_2O_3H (JCPDS card no. 40-1179), respectively, indicating the successful formation of the MoS_2/Ni_2O_3H composite. This result is in agreement with the HRTEM images. Moreover, the new presented peaks at 19.1° for (111) plane, 30.8° for (220) plane, 36.4° for (311), 54.6° for (422), 64.6° for (440) of the Co_3O_4 (JCPDS card no. 80-1545), and 24.14° for (012), 35.61° for (110), 53.79° for (116) and 63.91° for (300) plane of α-Fe_2O_3 (JCPDS card no. 33-0664) in MoS_2/Co_3O_4 and MoS_2/Fe_2O_3 samples, respectively, indicate the successful formation of the MoS_2/Co_3O_4 and MoS_2/Fe_2O_3 composites (**Figure 3** and **S10**).

The chemical compositions were further elucidated by the X-ray photoelectron spectroscopy (XPS). The XPS survey spectra in **Figure S11** clearly show the existence of the contained elements in all of the MoS_2 based composites, which are in great agreement with EDS mapping analyses. **Figure 3D-F** present the changes in the XPS patterns between the MoS_2/Ni_2O_3H, MoS_2/Co_3O_4 and MoS_2/Fe_2O_3 composites and their bare Ni_2O_3H, Co_3O_4 and Fe_2O_3 components. The peaks located at 854.5 eV and 871.9 eV are assigned to Ni $2p_{3/2}$ and Ni $2p_{1/2}$ binding energies of Ni^{2+} in Ni_2O_3H (Figure 3D).[27] It is worthwhile to point out that

these peaks shift to high binging energy at about 1.3 eV, which can be attributed to the electronic interaction between the Ni_2O_3H and MoS_2. XPS peak shifts were also observed in the MoS_2/Co_3O_4 and MoS_2/Fe_2O_3 composites compared with the bare Co_3O_4 and Fe_2O_3 components (Figure 3E and F), confirming the successful formation of the electronic coupled interface between the MoS_2 and corresponding metals oxides (Co_3O_4 and Fe_2O_3).[28-29]

In order to unveil the contributions of the metal oxides to the superior hydrogen evolution catalysis is the alkaline environment, the HER performance of the bare MoS_2, MoS_2/Ni_2O_3H, MoS_2/Co_3O_4 and MoS_2/Fe_2O_3 composite catalysts were conducted. The linear sweep voltammetry (LSV) curves shown in **Figure 4A** confirm that the HER catalytic activities of the MoS_2/Ni_2O_3H, MoS_2/Co_3O_4 and MoS_2/Fe_2O_3 composites are much higher than those of bare MoS_2, Ni_2O_3H, Co_3O_4 and Fe_2O_3 catalysts. This means the introduction of the metal oxides in the MoS_2 matrix effectively gives rise to HER activity in 1M KOH solution. Among all the catalysts, MoS_2/Ni_2O_3H presents the smallest overpotential of 84 mV at the current density of 10 mA/cm^2, which is 12, 49 and 120 mV lower than that of MoS_2/Co_3O_4 (96 mV), MoS_2/Fe_2O_3 (133 mV) and MoS_2 (204 mV), respectively. The current density on MoS_2/Ni_2O_3H at the overpotential of 200 mV can reach 217 mA/cm^2, which is about 1.7, 4.9, and 24 times higher than that of MoS_2/Co_3O_4 (131 mA/cm^2), MoS_2/Fe_2O_3 (44 mA/cm^2) and MoS_2 (9 mA/cm^2), respectively. This current density is even 2 times higher than that of the commercial Pt/C catalyst (110 mA/cm^2), indicating a superior catalyst to most previously reported earth abounded HER catalysts. Moreover, the electrochemical double layer capacitances (C_{dl}), which directly related to the electrochemically active surface area, was derived from the cyclic voltammetry curves in different scan rate (Figure S12). As shown in **Figure 4B**, there is no significant difference of C_{dl} for MoS_2/Ni_2O_3H (132.6 mF/cm^2),

MoS_2/Co_3O_4 (138.6 mF/cm^2) and MoS_2/Fe_2O_3 (114.2 mF/cm^2) catalysts than that of bare MoS_2 catalyst (102.5 mF/cm^2), indicating that the presence of the electronic coupled interfaces in the MoS_2 based composites plays a positive role in enhancing the intrinsic catalytic activity of HER in an alkaline environment. The calculated TOF of MoS_2/Ni_2O_3H, MoS_2/Co_3O_4 and MoS_2/Fe_2O_3 composite catalysts are 2.0 s^{-1}, 1.2 s^{-1} and 0.5 s^{-1} at the overpotential of 200 mV, respectively (Figure S13). It is worthy to notice that the TOF value of the MoS_2/Ni_2O_3H composite is 10 times higher than that of the bare MoS_2 nanosheet arrays (0.2 s^{-1}), indicating a significant enhancement of intrinsic HER activity for the MoS_2/Ni_2O_3H composite catalyst.

The Tafel curves and electrochemical impedance spectroscopy (EIS) Nyquist plots were further investigated to unveil the HER kinetics for the MoS_2, MoS_2/Ni_2O_3H, MoS_2/Co_3O_4 and MoS_2/Fe_2O_3 composite catalysts as shown in **Figure 4C-D**. The Tafel slopes of MoS_2, MoS_2/Ni_2O_3H, MoS_2/Co_3O_4 and MoS_2/Fe_2O_3 are measured to be 96.9, 82.3, 91.8 and 97.8 mV/dec, respectively, indicating a Volmer-Heyrovsky pathway on these four catalysts' surface.[12, 30] The charge-transfer resistances are extracted from the well-fitted Nyquist plots are 1.5, 2.6 and 7.4 Ω for the MoS_2/Ni_2O_3H, MoS_2/Co_3O_4 and MoS_2/Fe_2O_3 catalysts, respectively, which are all lower than that of bare MoS_2 (11.2 Ω). The electrochemical behavior of the MoS_2/metal oxide heterostructures demonstrates that the metal oxide decoration promotes the rate-limited water dissociation step, providing proton at the metal/oxide interface which then combines with a second proton to generated H_2.[9, 31] Obviously, the MoS_2/Ni_2O_3H composite exhibits the lowest charge-transfer resistance and Tafel slope, suggesting a highly kinetic HER catalyst in the base. Moreover, the practical hydrogen production rate in Figure S14 agreed well with the theoretical value, revealing that

approximately 100% of Faradic efficiency was attained. In order to better compare the HER kinetics with the recently reported highly active molybdenum-based catalysts in alkaline electrolyte, the key evaluation parameters, including overpotential, Tafel slope and C_{dl} were listed in Table S1. The HER performance of the MoS_2/metal oxides composites are markedly better than or at least comparable to those of the most active molybdenum-based HER catalysts in alkaline electrolyte.

The long-term stability of the MoS_2/Ni_2O_3H, MoS_2/Co_3O_4 and MoS_2/Fe_2O_3 composite catalysts were conducted via chronopotentiometry measurement at 10 mA/cm^2 for more than 45 hours (**Figure 5A**). There is no obvious increase in the overpotentials of these three catalysts during the long-term durability testing. In addition, we compare the polarization curves of the MoS_2/Ni_2O_3H, MoS_2/Co_3O_4 and MoS_2/Fe_2O_3 catalysts before and after the chronopotentiometry test, no dramatic change is detected for these catalysts (**Figure 5B-D**). Furthermore, we examined the surface morphologies and chemical composition of the MoS_2/Fe_2O_3 catalyst after performing the long-term stability testing. Evidently, almost no obvious changes are founded in the SEM and TEM images, and the EDS elemental analysis (**Figure S15-16**). These results show the excellent stability of the MoS_2/metal oxides composite catalysts in the alkaline environment.

We investigate the boosted HER performance by the interface construction with different transition metals oxides (**Figure 6**). The MoS_2/Ni_2O_3H interface exhibits the highest electroactivity for electron-transfer since the t_{2g}-e_g gap is significantly minimized and the e_g state obviously across E_F. These electronic distributions are also supported by the initial adsorption of the H_2O of HER in the base. The electroactive region largely facilitates the

adsorption of the H_2O. The shift of free H_2O to adsorbed H_2O gradually shrinks from MoS_2/Ni_2O_3H to MoS_2/Fe_2O_3, demonstrating the electron transfer capability. This is consistent with the electroactivity of the interface regions (**Figure 6A-C**). Then we analyze HER performance from an energetic perspective. Notably, MoS_2/Ni_2O_3H displays the strongest binding strength with the initial H_2O, guaranteeing a smooth activation of H_2O for the efficient HER (**Figure 6D**). The adsorption energies of H* near the interface are close for three different interfaces. However, the over-strong adsorption of H* is possible to result in the over-binding effect and lower the HER performances (**Figure 6E**). The electroactivity difference has further been proved through the energy barriers in the reaction coordinates. It is noted that MoS_2/Ni_2O_3H exhibits a barrier-free downhill reaction trend with a total energy release of -0.74 eV. The performance of MoS_2/Co_3O_4 is also superior with a slight barrier of 0.24 eV at the final releasement of H_2. For MoS_2/Fe_2O_3, though the initial reaction shows a much lower energy drop at the beginning of HER, the final releasement of formed H_2 experiences a very high energy barrier of 0.98 eV, which significantly reduces the HER performance (**Figure 6F**).

Conclusion

In summary, this work is the first demonstration of enhancing electrocatalytic HER performance in alkaline media by constructing MoS_2/Ni_2O_3H, MoS_2/Co_3O_4 and MoS_2/Fe_2O_3 heterostructures. The outstanding enhancement of the HER electrocatalytic activity for these MoS_2/metal oxide heterostructures is related to the electronic coupled interfaces between MoS_2 and metal oxides catalysts. Among all of the MoS_2/metal oxide composite catalysts, the as-obtained MoS_2/Ni_2O_3H catalyst yield the highest HER activity with an overpotential as low as 84 mV at 10 mA/cm^2 and charge-transferred resistance of 1.5 Ω at the overpotential of 200

mV in alkaline electrolyte, along with high long-term stability. Moreover, the MoS_2/Ni_2O_3H catalyst achieves a current density of 217 mA/cm^2 at the overpotential of 200 mV, which is 2 times higher than that of the commercial Pt/C catalyst in alkaline media, indicating a superior earth-abounded catalyst to the state-of-the-art HER catalysts. Detailed theoretical calculations unveil the sensitivity of different 3d-orbitals towards the interface modulations, which significantly excite the Ni-3d bands in MoS_2/Ni_2O_3H to actualize the fast electron transfer for highly efficient alkaline HER. By appropriate selection of transition oxides, the flexible control of the electroactivity for HER is able to achieve, which supplies novel insights in fabricating highly electroactive composite catalysts.

Experimental Section

Material synthesis. All chemicals are of analytical grade and were used as received without further purification. Ultrapure deionized water (18.2 MΩ/cm) was used in all experiments. Carbon fiber paper (HCP020P, Hesen) was first immersed in 98% H_2SO_4 (Sigma-Aldrich) for 1 hour to remove the residual metal on the surface.

Synthesis of vertical MoS_2 arrays. The vertically aligned MoS_2 nanosheet arrays were prepared using the method reported in our previous paper.[24] In a typical synthesis procedure, 671 mg sodium molybdate dihydrate (>99.5%, Sigma-Aldrich) was dissolved in 40 ml N_2-saturated water. Then 225 mg thioacetamide (>99%, Sigma-Aldrich) was added into the beaker with dissolved sodium molybdate dihydrate solution. After stirring the mixture for half an hour under continuous N_2 flow, the mixed solution was transferred to a 100 ml Teflon vessel, and then one piece of cleaned carbon fiber paper (HCP020P, Hesen) was immersed in the mixture. The Teflon vessel was sealed and maintained at 200 ºC for 2 h in a microwave hydrothermal system (2.45 GHz, Ethos one, Milestone Inc.) with accurately monitoring and controlling the internal temperature within ±5º. Then the reaction mixture was cooled to room

temperature at the speed of 20 ºC/min. The product was washed with ultrapure deionized water for several times, and then sonicated for at least 30 min to remove the weakly bonded MoS_2 from the surface, and lastly dried in the vacuum oven at the temperature of 60 ºC.

Synthesis of MoS_2/Ni_2O_3H, MoS_2/Co_3O_4 and MoS_2/Fe_2O_3. In a typical synthesis, 1.2 ml 1 M nickel nitrate ($Ni(NO_3)_2$) aqueous solutions were added into 40 ml N_2-saturated water. Then 3 ml 1 M urea and 0.2 ml 0.1 M trisodium citrate aqueous solutions were added into the beaker with the mixed solution. After stirring the mixture for half an hour under continuous N_2 flow, the mixed solution was transferred to a 100 ml Teflon vessel, and then one piece of carbon fiber paper with as-synthesized MoS_2 was immersed in the mixture. The Teflon vessel was sealed and maintained at room temperature for 2 h, followed by hydrothermal treatment at 120 ºC for 12 h. The product was washed with ultrapure deionized water for several times. Ni_2O_3H was synthesized by the same procedure of MoS_2/Ni_2O_3H synthesis with the only difference of without MoS_2 precursor. MoS_2/Co_3O_4 and MoS_2/Fe_2O_3 were synthesized by the same procedure of MoS_2/Ni_2O_3H synthesis with different precursors. MoS_2/Co_3O_4 was synthesized with 1.2 ml 1 M cobalt chloride ($Co(NO_3)_2$), while MoS_2/Fe_2O_3 was synthesized with 1.2 ml 1 M cobalt chloride ($Fe(NO_3)_3$) instead of nickel nitrate.

The loading of the as-obtained MoS_2 nanostructure for all the MoS_2 hybrids, which were accurately measured by weighing the dry carbon fiber paper before and after synthesis process, is about 3 mg/cm^2 and the loadings of Ni_2O_3H, Co_3O_4, and Fe_2O_3 for all of the MoS_2 composites are 1.8 mg/cm^2, 2.6 mg/cm^2 and 0.5 mg/cm^2, respectively.

Characterization. The morphology of the as-synthesized samples was determined by using field-emission scanning electron microscopy (FESEM) which was characterized by a JEOL JSM-7100F at an accelerating voltage of 10 kV.

Transmission electron microscope (TEM), selected area electron diffraction (SAED) and energy-disperse X-ray spectrum (EDS) were taken with a JEOL-2010 with an acceleration voltage of 200 kV. High resolution transmission electron microscope (HRTEM) images were captured on JEOL-2010F instrument microscopy at an accelerating voltage of 200 kV.

The as-synthesized samples were examined by X-ray powder diffraction (XRD) which was carried out on a Philips PW-1830 X-ray diffractometer with Cu Kα radiation (K=0.15418 nm).

Raman spectra were performed using a Raman microscope Renishaw 2000 excited with a 514 nm argon ion laser of 2mm spot size excitation.

X-ray photoelectron spectroscopy (XPS) were measured on a Perkin-Elmer model PHI 5600 XPS system with a resolution of 0.3–0.5 eV from a monochromated aluminum anode X-ray source with MoKα radiation (1486.6 eV).

Electrocatalytic study. Electrochemical measurements of the as-synthesized samples were performed with a CHI 760E electrochemistry workstation (Shanghai Chenhua Instrument, Inc.) using a standard three-electrode electrochemical cell with carbon rod and Hg/HgO as the counter and the reference electrode, respectively. Electrochemically inert tape was used to define the 1 cm^2 electrode area. The electrochemical measurements were all performed at room temperature, and the potential was referenced to that of the reversible hydrogen electrode (RHE). For the RHE calibration, the potential difference between Hg/HgO and RHE was measured in a cell where Pt foil was used as the working electrode and Hg/HgO was used as the counter and reference electrodes in a 99.999% pure H_2-saturated 1 M KOH aqueous solution. During the measurement, high-purity H_2 is bubbled into the electrolyte to saturate the electrolyte and fix the reversible hydrogen potential. The open-circuit potential was recorded from an open circuit potential-time curve. Cyclic voltammograms (CVs) were taken several cycles to bubble away the surface contaminates and at the same time stabilize the

catalysts. The polarization curves were obtained by linear sweeping with a scan rate of 5 mV/s in the H_2-saturated 1 M KOH aqueous solution. All the polarization curves were *iR*-corrected, except as otherwise noted. The *iR*-corrected potential, $E_{iR\text{-free}}$, is determined directly from the experimentally measured solution resistance (R_s) follow the equation: $E_{iR-\text{free}} = E - iR_s$. Double layer capacitance (C_{dl}) was estimated by the CV cures at various scan rates in the potential region of 0.1~ 0.2 V vs. RHE. Electrochemical impedance spectroscopy (EIS) was performed at the overpotential of 200 mV over a frequency range from 100 kHz to 10 mHz at the amplitude of the sinusoidal voltage of 10 mV.

Calculation Setup. We choose the density functional theory (DFT) within the CASTEP codes to perform all the theoretical calculations [32]. The generalized gradient approximation (GGA) and Perdew-Burke-Ernzerhof (PBE) for the exchange-correlation energy with the 380 eV cutoff energy have been applied [33-35]. The ultrasoft pseudopotential scheme has been chosen [36] with the valence treatment as (*1s*), (*2s, 2p*), (*3d, 4s, 4p*), (*3d, 4s, 4p*), (*3d, 4s, 4p*) and (*4d, 5s, 5p*) as the valence states for H, O, Ni, Co, Fe, and Mo, respectively. For all the geometry optimizations, the Hellmann-Feynman forces will be converged to less than 0.001 eV/Å while the total energy has been converged to 5×10^{-5} eV per atom. The Gamma k-point has been applied for the energy minimization based on the Broyden-Fletcher-Goldfarb-Shannon (BFGS) algorithm [37-38]. The MoS_2/Ni_2O_3H interface model is constructed by cleavage of (002) surface of MoS_2 and (101) surface of Ni_2O_3H. The MoS_2/Co_3O_4 interface model is constructed by cleavage of (002) surface of MoS_2 and (311) surface of Co_3O_4. The MoS_2/Fe_2O_3 is constructed by cleavage of (002) surface of MoS_2 and (012) surface of Fe_2O_3. For a full relaxation of the local lattice within adsorption, a 15 Å vacuum space along z-direction to supply sufficient space is introduced.

Supporting Information

Supporting Information is available from the Wiley Online Library or from the author.

Acknowledgements

This research is supported by National Nature Science Foundation of China (Nos. 21862011, 51864024, 21771156) and Yunnan province (2019FI003), the Kunming University of Science and Technology (Nos. KKKP201707010, KKKP201752011), the Shenzhen Knowledge Innovation Program (Basic Research, JCYJ20190808181205752) and the Early Career Scheme (ECS) fund (Grant No.: PolyU 253026/16P) from the Research Grant Council (RGC) in Hong Kong.

Received: ((will be filled in by the editorial staff))
Revised: ((will be filled in by the editorial staff))
Published online: ((will be filled in by the editorial staff))

References

[1] Z. W. Seh; J. Kibsgaard; C. F. Dickens; I. Chorkendorff; J. K. Nørskov; T. F. Jaramillo, *Science* **2017,** *355* (6321).

[2] J. Hu; L. Wu; K. A. Kuttiyiel; K. R. Goodman; C. Zhang; Y. Zhu; M. B. Vukmirovic; M. G. White; K. Sasaki; R. R. Adzic, *J. Am. Chem. Soc.* **2016,** *138* (29).

[3] P. De Luna; C. Hahn; D. Higgins; S. A. Jaffer; T. F. Jaramillo; E. H. Sargent, *Science* **2019,** *364* (6438).

[4] C. Zhang; J. Hu; W. Fan; M. K. H. Leung; Y. Meng, *Electrochimica Acta* **2016,** *204*.

[5] X. Zhao; W. Cai; Y. Yang; X. Song; Z. Neale; H.-E. Wang; J. Sui; G. Cao, *Nano Energy* **2018,** *47*.

[6] X. Zhao; Y. Zhao; B. Huang; W. Cai; J. Sui; Z. Yang; H.-E. Wang, *Chem. Eng. J.* **2020,** *382*.

[7] D. Strmcnik; M. Uchimura; C. Wang; R. Subbaraman; N. Danilovic; V. van der; A. P. Paulikas; V. R. Stamenkovic; N. M. Markovic, *Nat. Chem.* **2013,** *5* (4).

[8] J. Hu; C. Zhang; X. Meng; H. Lin; C. Hu; X. Long; S. Yang, *J. Mater. Chem. A* **2017,** *5* (13).

[9] C.-T. Dinh; A. Jain; F. P. G. de Arquer; P. De Luna; J. Li; N. Wang; X. Zheng; J. Cai; B. Z. Gregory; O. Voznyy; B. Zhang; M. Liu; D. Sinton; E. J. Crumlin; E. H. Sargent, *Nat. Energy* **2019,** *4* (2).

[10] J. Lai; B. Huang; Y. Chao; X. Chen; S. Guo, *Adv. Mater.* **2019,** *31* (2).

[11] D. Li; Y. Jia; G. Chang; J. Chen; H. Liu; J. Wang; Y. Hu; Y. Xia; D. Yang; X. Yao, *Chem* **2018,** *4* (10).

[12] J. Durst; A. Siebel; C. Simon; F. Hasche; J. Herranz; H. A. Gasteiger, *Energy Environ. Sci.* **2014,** *7* (7).

[13] Y. Zheng; Y. Jiao; A. Vasileff; S.-Z. Qiao, *Angew. Chem. Int. Ed.* **2018,** *57* (26).

[14] K. Elbert; J. Hu; Z. Ma; Y. Zhang; G. Chen; W. An; P. Liu; H. S. Isaacs; R. R. Adzic; J. X. Wang, *ACS Catal.* **2015,** *5* (11).

[15] J. Hu; C. Zhang; P. Yang; J. Xiao; T. Deng; Z. Liu; B. Huang; M. K. H. Leung; S. Yang, *Adv. Funct. Mater.* **2020,** *30* (6).

[16] C. G. Morales-Guio; L. A. Stern; X. L. Hu, *Chem. Soc. Rev.* **2014,** *43* (18).

[17] J. Hu; K. A. Kuttiyiel; K. Sasaki; C. Zhang; R. R. Adzic, *J. Electrochem. Soc.* **2018,** *165* (15).

[18] D. Voiry; H. S. Shin; K. P. Loh; M. Chhowalla, *Nature Rev. Chem.* **2018,** *2*.

[19] J. Hu; C. Zhang; L. Jiang; H. Lin; Y. An; D. Zhou; M. K. H. Leung; S. Yang, *Joule* **2017,** *1* (2).

[20] R. Subbaraman; D. Tripkovic; D. Strmcnik; K.-C. Chang; M. Uchimura; A. P. Paulikas; V. Stamenkovic; N. M. Markovic, *Science* **2011,** *334* (6060).

[21] N. Danilovic; R. Subbaraman; D. Strmcnik; K.-C. Chang; A. P. Paulikas; V. R. Stamenkovic; N. M. Markovic, *Angew. Chem.* **2012,** *124* (50).

[22] P. Wang; X. Zhang; J. Zhang; S. Wan; S. Guo; G. Lu; J. Yao; X. Huang, *Nat. Comm.* **2017,** *8*.

[23] T. Sun; L. Xu; Y. Yan; A. A. Zakhidov; R. H. Baughman; J. Chen, *ACS Catal.* **2016,** *6* (3).

[24] J. Hu; B. Huang; C. Zhang; Z. Wang; Y. An; D. Zhou; H. Lin; M. K. H. Leung; S. Yang, *Energy Environ. Sci.* **2017,** *10* (2).

[25] C. Zhang; L. Jiang; Y. Zhang; J. Hu; M. K. H. Leung, *J. Catal.* **2018,** *361*.

[26] X. Zhao; Y. Zhao; B. Huang; Z. Yang; W. Cai; J. Sui; G. Cao; H.-E. Wang, *J. Power Sources* **2020,** *446*.

[27] Z. Zhu; H. Yin; C.-T. He; M. Al-Mamun; P. Liu; L. Jiang; Y. Zhao; Y. Wang; H.-G. Yang; Z. Tang; D. Wang; X.-M. Chen; H. Zhao, *Adv. Mater.* **2018,** *30* (28).

[28] Z. Wang; X. Ren; X. Shi; Abdullah M. Asiri; L. Wang; X. Li; X. Sun; Q. Zhang; H. Wang, *J. Mater. Chem. A* **2018,** *6* (9).

[29] J. Zhang; T. Wang; D. Pohl; B. Rellinghaus; R. Dong; S. Liu; X. Zhuang; X. Feng, *Angewandte Chemie International Edition* **2016,** *55* (23).

[30] D. Merki; H. Vrubel; L. Rovelli; S. Fierro; X. Hu, *Chem. Sci.* **2012,** *3* (8).

[31] M. Gong; W. Zhou; M. J. Kenney; R. Kapusta; S. Cowley; Y. Wu; B. Lu; M.-C. Lin; D.-Y. Wang; J. Yang; B.-J. Hwang; H. Dai, *Angew. Chem. Int. Ed.* **2015,** *54* (41).

[32] S. J. Clark; M. D. Segall; C. J. Pickard; P. J. Hasnip; M. J. Probert; K. Refson; M. C. Payne, *Zeitschrift Fur Kristallographie* **2005,** *220* (5-6).

[33] J. P. Perdew; K. Burke; M. Ernzerhof, *Phys Rev Lett* **1996,** *77* (18).

[34] P. J. Hasnip; C. J. Pickard, *Comput Phys Commun* **2006,** *174* (1).

[35] J. P. Perdew; J. A. Chevary; S. H. Vosko; K. A. Jackson; M. R. Pederson; D. J. Singh; C. Fiolhais, *Physical Review B* **1992,** *46* (11).

[36] D. Vanderbilt, *Physical Review B* **1990,** *41* (11).

[37] J. D. Head; M. C. Zerner, *Chem Phys Lett* **1985,** *122* (3).

[38] M. I. J. Probert; M. C. Payne, *Physical Review B* **2003,** *67* (7).

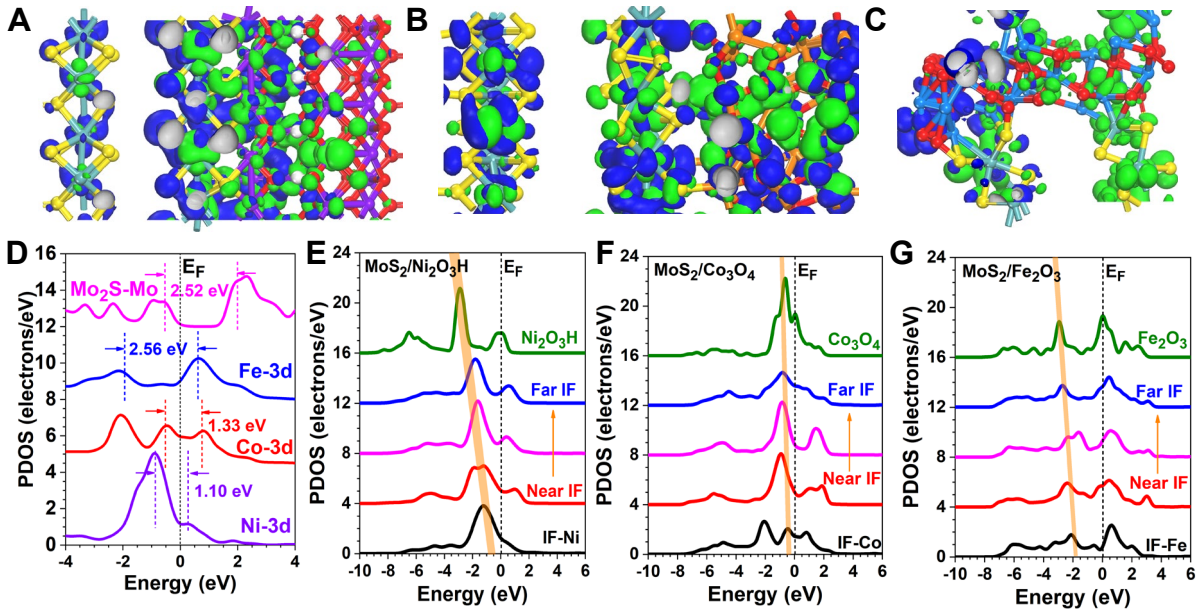

Figure 1. The real spatial contour plots for bonding and anti-bonding orbitals near E_F for the (**A**) MoS_2/Ni_2O_3H, (**B**) MoS_2/Co_3O_4, and (**C**) MoS_2/Fe_2O_3. Cyan Balls = Mo, Yellow balls = S, Purple Balls= Ni, Orange Balls= Co, Blue Balls = Fe, Red Balls = Oxygen, White Balls = H. (**D**) PDOSs of 3d bands of MoS_2/Ni_2O_3H, MoS_2/Co_3O_4, and MoS_2/Fe_2O_3. (**E**) Site-

dependent 3d-band of Ni in MoS_2/Ni_2O_3H. (**F**) Site-dependent 3d-band of Co in MoS_2/Co_3O_4. (**G**) Site-dependent 3d-band of Fe in MoS_2/Fe_2O_3.

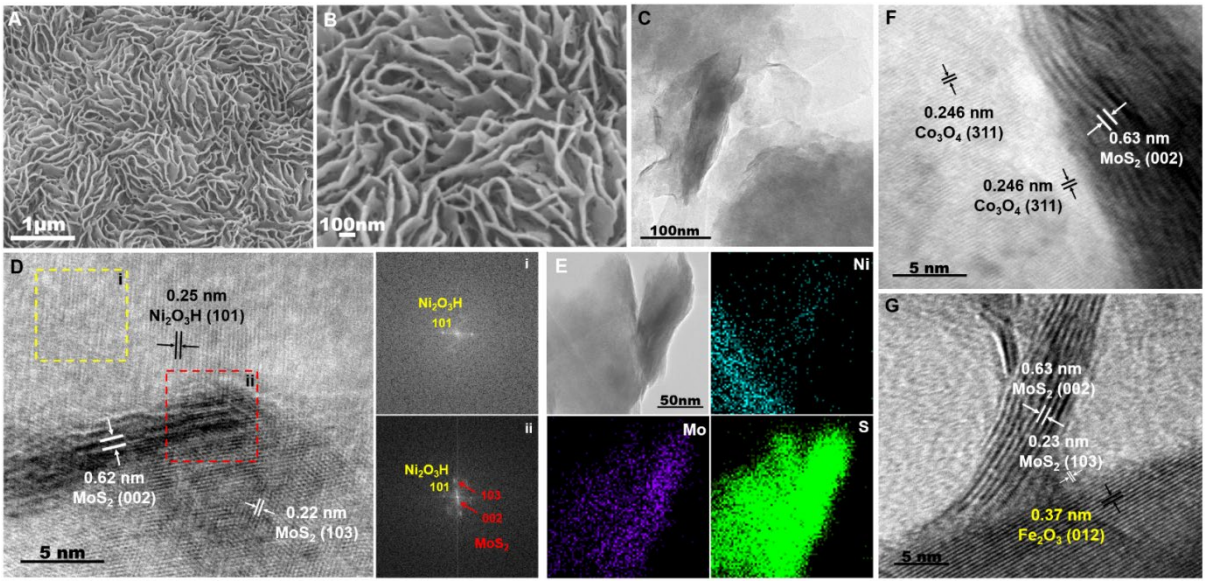

Figure 2. Morphology of the MoS_2/Ni_2O_3H composite. (**A**) Low- and (**B**) high-magnification FESEM images of MoS_2/Ni_2O_3H. (**C**) TEM and (**D**) HRTEM images of the MoS_2/Ni_2O_3H composite. (i and ii) The corresponding fast FFT patterns of the selected areas marked by dash square. (**E**) TEM image and the corresponding energy-dispersive spectroscopy (EDS) mapping profiles for Ni, Mo, and S of MoS_2/Fe_2O_3 composite. HRTEM images of the (F) MoS_2/Co_3O_4 and (G) MoS_2/Fe_2O_3 composites.

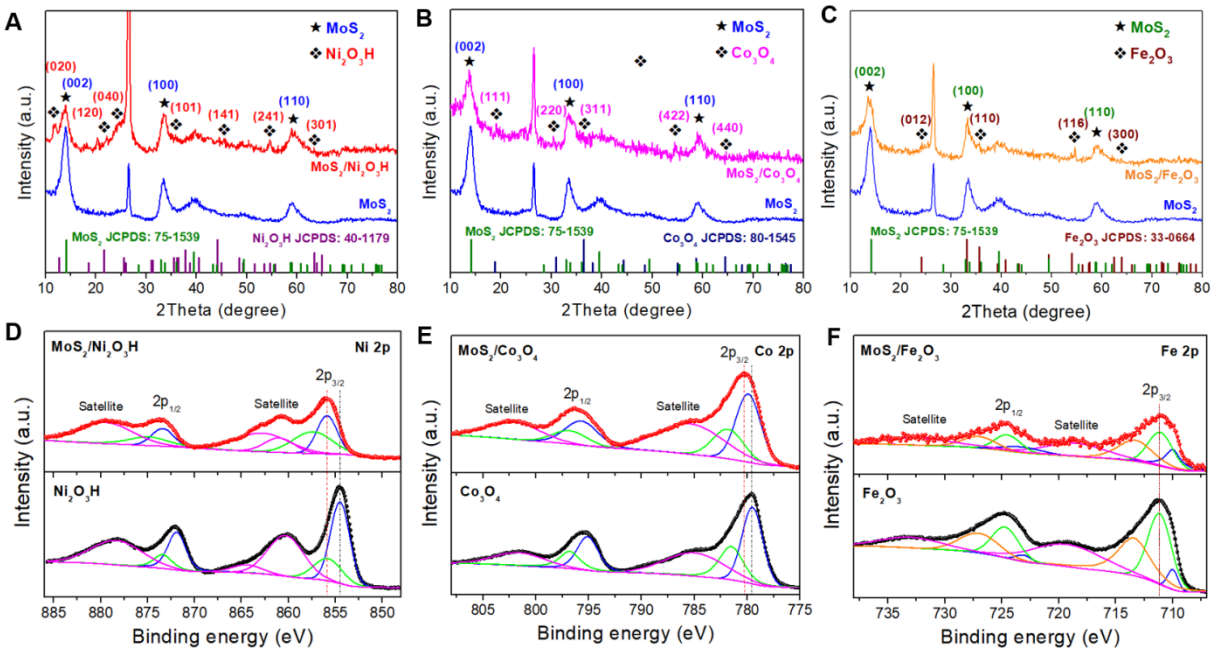

Figure 3. Chemical structure of the MoS_2/Ni_2O_3H, MoS_2/Co_3O_4 and MoS_2/Fe_2O_3 composites. XRD patterns of the (**A**) MoS_2/Ni_2O_3H, (**B**) MoS_2/Co_3O_4 and (**C**) MoS_2/Fe_2O_3, together with the standard pattern of 2H MoS_2 (JCPDS 75-1539), Ni_2O_3H (JCPDS 40-1179), Co_3O_4 (JCPDS 80-1545) and Fe_2O_3 (JCPDS 33-0664). (**D**) X-ray photoelectron spectra Ni 2p of the MoS_2/Ni_2O_3H and Ni_2O_3H. (**E**) X-ray photoelectron spectra Co 2p of the MoS_2/ Co_3O_4 and Co_3O_4. (**F**) X-ray photoelectron spectra Fe 2p of the MoS_2/Fe_2O_3 and Fe_2O_3.

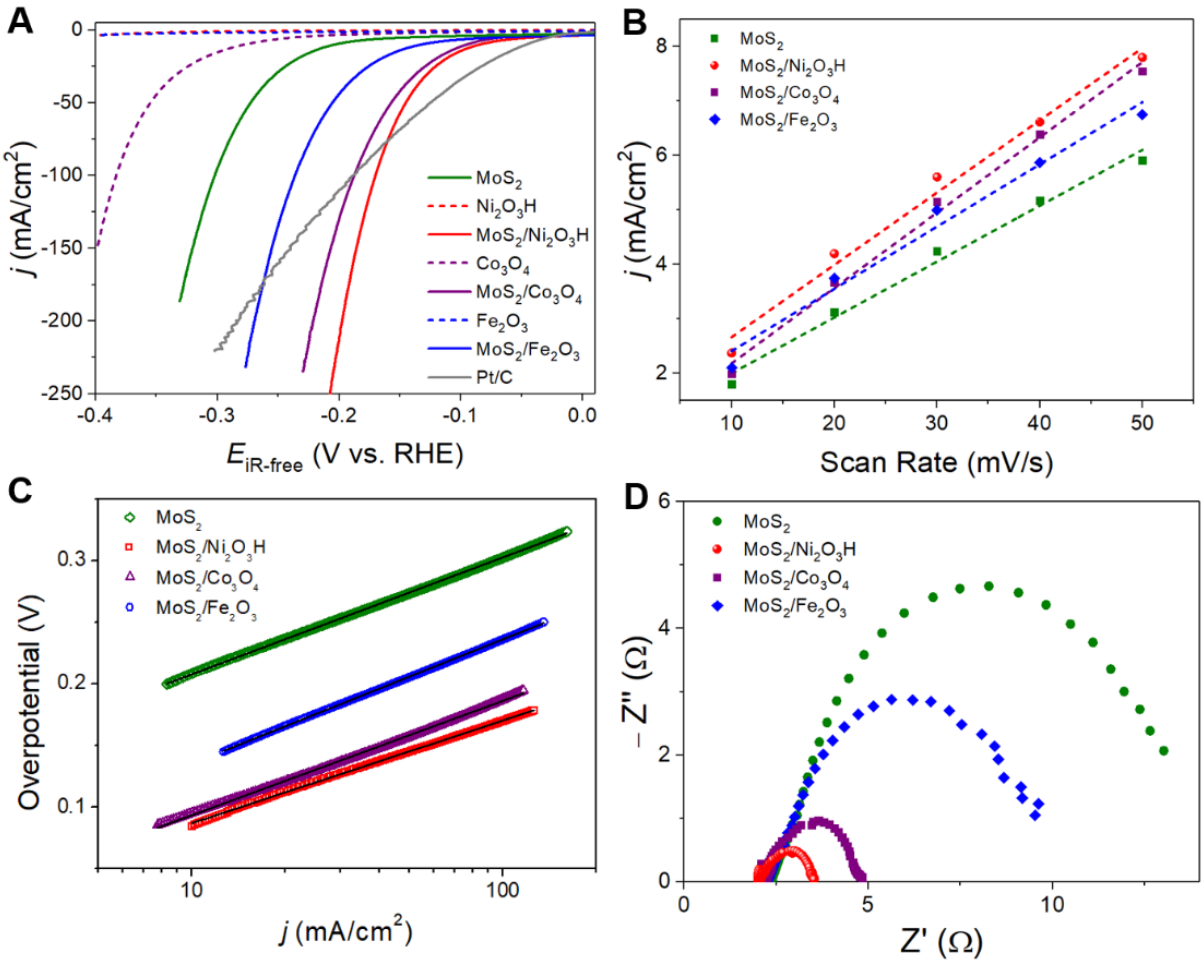

Figure 4. Electrocatalytic properties of the MoS_2/Ni_2O_3H, MoS_2/Co_3O_4 and MoS_2/Fe_2O_3 composites. (**A**) Polarization curves and (**B**) Tafel plots of the bare MoS_2, Ni_2O_3H, Co_3O_4, Fe_2O_3, and the MoS_2/Ni_2O_3H, MoS_2/Co_3O_4, MoS_2/Fe_2O_3 composite catalysts in 1M KOH solution at a scan rate of 5 mV/s. (**C**) Charging current density differences plotted against scan rate of the MoS_2, MoS_2/Ni_2O_3H, MoS_2/Co_3O_4 and MoS_2/Fe_2O_3 composite catalysts. (**D**) Nyquist plots of the MoS_2, MoS_2/Ni_2O_3H, MoS_2/Co_3O_4 and MoS_2/Fe_2O_3 composite catalysts at the overpotential of 200 mV.

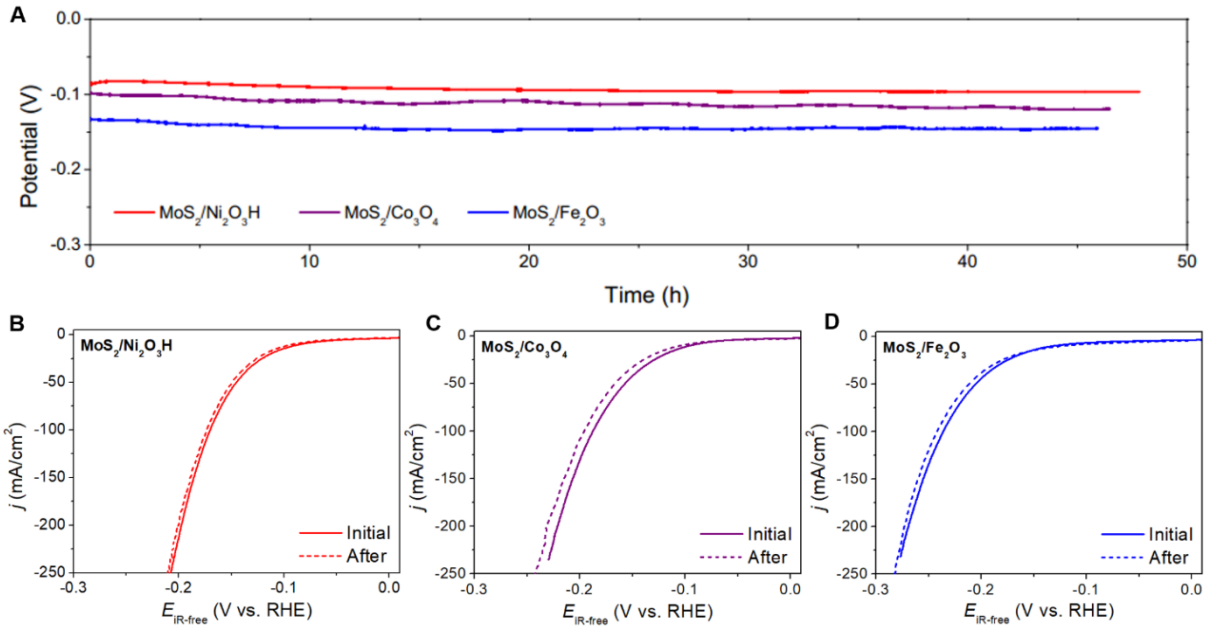

Figure 5. Electrocatalytic stability of the MoS_2, MoS_2/Ni_2O_3H, MoS_2/Co_3O_4 and MoS_2/Fe_2O_3 composites. (**A**) Chronopotentiometry responses ($\eta \sim t$) recorded from MoS_2/Fe_2O_3 composite at the current densities of -10 mA/cm^2 for more than 46 h. Polarization curves recorded from (**B**) MoS_2/Ni_2O_3H, (**C**) MoS_2/Co_3O_4 and (**D**) MoS_2/Fe_2O_3 composites at a scan rate of 5 mV/s before (solid curve) and after (dotted curve) the chronopotentiometry test.

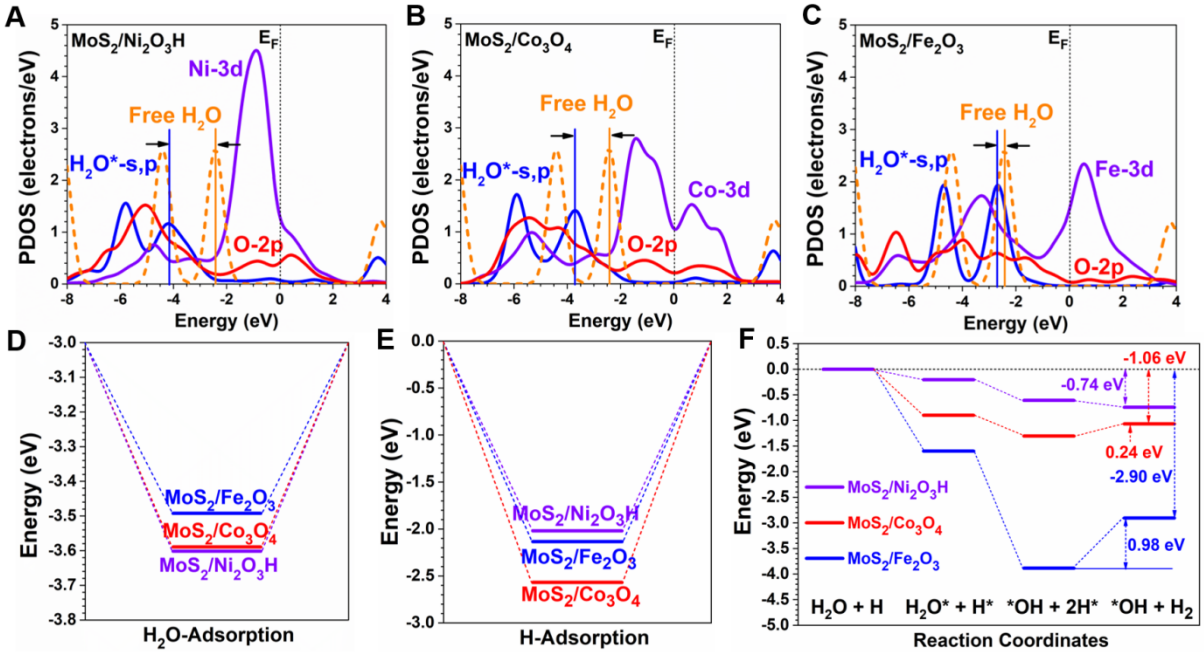

Figure 6. PDOSs of H_2O adsorption on (**A**) MoS_2/Ni_2O_3H, (**B**) MoS_2/Co_3O_4, and (**C**) MoS_2/Fe_2O_3. The adsorption energies comparison of (**D**) H_2O and (**E**) H* for HER. (**F**) The energetic pathway of HER under the alkaline condition.

Through the interfacial engineering, the earth-abundant MoS_2 based catalyst has been synthesized with the transition metal oxides. With the optimized electroactive interfaces with efficient electron transfer, the low overpotential for HER in the alkaline is realized in MoS_2/Ni_2O_3H with long-term durability. This indicates a new strategy of developing superior catalysts for HER in the harsh alkaline environment.

Keyword: Interfacial Engineering

J. Hu, C. Zhang, Y. Zhang, B. Yang, Q. Qi, M. Sun, F. Zi, M. K. H. Leung, and B. Huang

Interface modulation of MoS_2/metal oxide heterostructures for efficient hydrogen evolution electrocatalysis